Arctic lead detection using a waveform mixture algorithm from CryoSat-2 data

Sanggyun Lee[1], Hyun-Cheol Kim[2], and Jungho Im[1,3,*]

[1]School of Urban and Environmental Engineering, Ulsan National Institute of Science and Technology (UNIST), Ulsan, 44949, South Korea
[2]Unit of Arctic Sea-Ice prediction, Korea Polar Research Institute (KOPRI), Incheon, 21990, South Korea
[3]Environmental Resource Engineering, State University of New York, College of Environmental Science and Forestry, 13210, Syracuse, NY, USA

Correspondence to: Jungho Im (ersgis@unist.ac.kr)

Abstract. Arctic sea ice leads play a major role in exchanging heat and momentum between the Arctic atmosphere and ocean as well as in the retrieval of sea ice thickness. Although leads cover only a small portion of the Arctic Ocean, they affect the heat budget in the Arctic region considerably. In this study, we propose a waveform mixture analysis to detect leads, which is novel and different from the existing threshold-based lead detection methods. The waveform mixture analysis adopts the concept of linear mixture analysis that is widely used in the field of hyperspectral image analysis. This lead detection method based on the waveform mixture analysis was evaluated with high resolution (250m) MODIS images and showed better performance in detecting leads than previous methods. The robustness of the proposed approach also lies in the fact that it does not require the rescaling of parameters, as it directly uses L1B waveform data unlike the existing threshold-based methods. Monthly lead fraction maps derived by the waveform mixture analysis were produced, which show a strong inter-annual variability of recent sea ice cover during 2006-2011 excluding the summer season (i.e., June to September). We also compared the lead fraction maps to other lead fraction maps generated from the literature, resulting in similar spatiotemporal patterns.

1 Introduction

Sea ice leads (hereafter known as "leads"), linearly elongated cracks between sea ices, are a common feature in the Arctic Ocean during spring and winter seasons. Leads facilitate a large amount of heat and moisture exchanges between the atmosphere and the ocean because of the huge temperature differences between them (Maykut. 1982; Perovich et al., 2011). Although leads occupy a small portion of the Arctic Ocean, there is much more heat transfer between the atmosphere and ocean through leads than sea ice (Maykut, 1978; Marcq and Weiss, 2012). Furthermore, Lupkes et al. (2008) showed that a 1% change in sea ice concentration owing to an increase of lead fraction could make near surface temperature up to a 3.5 K in the Arctic. Thus, the detection and monitoring of leads in the Arctic Ocean are crucial because they are closely related to the Arctic heat budget and the physical interaction between the atmospheric boundaries and sea ice in the Arctic.

Satellite sensors have been the most efficient way to monitor leads in the entire Arctic region since the 1990s (Key et al., 1993; Lindsay and Rothrock, 1995; Miles and Barry, 1998). Advanced Very High Resolution Radiometer (AVHRR) and Defense Meteorological Satellite Program (DMSP) satellite visible and thermal images were used to detect leads in the early 1990s. Recently, Moderate Resolution Imaging Spectroradiometer (MODIS) Ice Surface Temperature (IST) product, with 1km

5 spatial resolution, was used to detect leads to map pan-Arctic lead presence (Willmes and Heinemann, 2015; Willmes and Heinemann, 2016). They mitigated cloud interference using a fuzzy cloud artefact filter and investigated lead dynamics based on a comparison between pan-Arctic lead maps and the characteristics of the Arctic Ocean such as shear zones, bathymetry, and currents. While optical sensors have a finer spatial resolution, they are not pragmatic in the dark regions during polar nights (from December to February). In addition, leads are easily contaminated by clouds. Microwave instruments such as

10 passive microwave sensors and altimeters have been used to detect leads and produced lead fractions. Rohrs and Kaleschke (2012) utilized the polarization ratio of Advanced Microwave Scanning Radiometer for EOS (AMSR-E) and retrieved daily thin ice concentration. With the help of the thin ice concentration, lead orientations and frequencies were derived using an image analysis technique (i.e., Hough transform) (Brohan and Kaleschke, 2014). A radar altimeter could detect leads as well. Zygmuntowska et al. (2013) used Airborne Synthetic Aperture and Interferometric Radar Altimeter System (ASIRAS), similar

15 to CryoSat-2, to identify leads based on waveform characteristics and a Bayesian classifier. While Zakharova et al. (2015) applied simple thresholds to identify leads along with Satellite with Argos and Altika (SARAL/Altika) tracks and estimated regional lead fractions, Wernecke and Kaleschke (2015) optimized thresholds to detect leads and produced pan-Arctic lead fraction maps using CryoSat-2 with the analysis of lead width, and sea surface height.

Linear mixture analysis, based on the assumption that the spectra measured by sensors for a pixel is a linear combination

20 of the spectra for all components within the pixel (Keshava and Mustard, 2002) was first applied to the altimetry research field in the Polar Region by Chase and Hoyer (1990). They estimated sea ice type and concentration using linear mixture analysis based on Geosat waveforms. However, the Geosat with a relatively small number of bins and coarser spatial resolution is not enough to detect small leads in the winter and spring seasons in the Arctic. In this study, we adopted the linear mixture analysis concept to waveforms from the SAR radar altimeter, CryoSat-2, to identify leads and produced monthly pan-Arctic lead

25 fractions in January to May and October to December between 2011 and 2016. Waveform endmembers that are crucial to implement linear mixture analysis were extracted by the N-FINDR (N-finder) algorithm, which can mitigate the subjective selection of endmembers. The detected leads were visually evaluated with MODIS images (at 250 m resolution) and compared with other thresholds based lead detection methods. The lead detection of waveform mixture analysis is not easily affected by the update of the CryoSat-2 baseline, which is novel and different from previous threshold based lead detection methods. The

30 main objectives of this study are to 1) develop a novel lead detection method based on waveform mixture analysis, 2) identify recent pan-Arctic lead fractions, and 3) investigate the relationship between Arctic lead fraction and thermodynamics and ice dynamics.

2. Data

2. 1 CryoSat-2

CryoSat-2, carrying Synthetic Aperture Interferometric Radar Altimeter (SIRAL) was launched in September 2010 by the European Space Agency (ESA). CryoSat-2 is a satellite dedicated to Polar research. SIRAL is a radar altimeter with a central
5   frequency of 13.575 GHz (K_u-band) and a bandwidth of 320 MHz. CryoSat-2 takes an advantage of SIRAL to detect smaller leads (e.g., ~ 300 m) with an efficient use of the instrument's energy compared to the previous radar altimeter missions such as GeoSat and Jason (Wingham et al., 2006). In this study, we used the SAR and SIN of level 1b baseline C data, which has 256 and 1024 range bins, respectively (Scagliola, 2014).

CryoSat-2 transmits burst of radar pulses (i.e., 64) with high Pulse Repetition Frequency (PRF) (i.e., 18.181kHz), which
10   forms Doppler beams because of the along-track movement of the satellite (Wingham et al., 2006). With the help of the high PRF, each Doppler beam is coherently correlated and pointed at the same location on the Earth surface. This is called beam stacking. The stacking beams are averaged to reduce speckle and thermal noise and this is called multi-looking (Salvatore. 2013). The results in the waveforms in the L1b SAR data are shown in Fig. 1. Such a waveform represents temporal distribution of reflected power when the radar pulses reach the surface with a condition (e.g., flat or rough surface). In this case, since the
15   leading edge of each waveform starts from a different range bin, the beginning of the waveform was set at 1% of the maximum echo power (Figure 1). For more detailed explanation about processes to develop L1b waveform data, refer to Salvatore (2013).
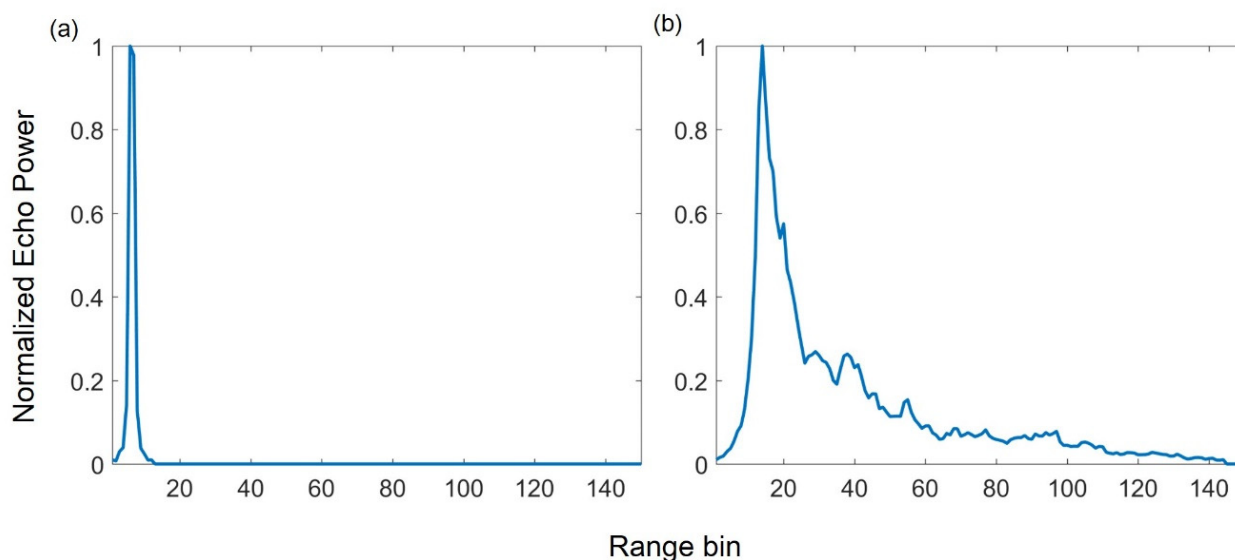
Figure 1: Representative waveforms of (a) leads and (b) sea ice over the Arctic Ocean selected by N-FINDR algorithm during January to May and October to December between 2011 and 2016. Refer to the methods section for N-FINDR algorithm.

2.2 Sea ice edge data

The European organization for the exploitation of METeorological SATellites (EUMETSAT) Ocean and Sea Ice Satellite Application Facility (OSI SAF) provides multiple sea ice products such as sea ice concentration, sea ice edge, sea ice type, sea ice emissivity, and sea ice drift. The sea ice edge product was developed using the polarization ratio of 19 GHz and

5   91 GHz, the spectral gradient ratio of 37 GHz and 19 GHz from Special Sensor Microwave Imager/Souder (SSMIS), and anisFMB from The Advanced Scatterometer (ASCAT) with Bayesian approach (Aaboe et al., 2016). In this study, monthly averaged sea ice edge data was used to mask out monthly lead fraction maps. The open ice cover in the sea ice edge product was regarded as an open ocean.

2.3 Monthly lead fraction maps

10   Lead fraction maps produced from previous studies (Rohrs and Kaleschke, 2012; Wernecke and Kaleschke, 2015; Willmes and Heinemann, 2016) were used to compare to the lead fraction maps generated using the proposed waveform mixture analysis in this study. Rohrs and Kaleschke (2012) produced daily thin ice concentration maps using AMSR-E data with a 6.25 km grid, which can detect leads that are wider (i.e., width) than 3 km. The daily thin ice concentration that was over 0.5 (i.e., 50%) was considered to be a lead and binary daily lead maps were averaged to properly compare other monthly lead fraction

15   maps. A threshold optimization based lead detection method with the CryoSat-2 was used in Wernecke and Kaleschke (2015) and monthly lead fraction maps were calculated with the grids of 99.5 km. The thin ice concentration maps (Rohrs and Kaleschke, 2012) and the lead fraction maps using CryoSat-2 (Wernecke and Kaleschke, 2015) are available on their website (http://icdc.cen.uni-hamburg.de/1/daten/cryosphere.html). Willmes and Heinemann (2016) also produced daily lead maps over the entire Arctic Region, classifying land, cloud, sea ice, lead-artefact, and lead fraction maps using MODIS data with the

20   spatial resolution less than 2 km. The lead-artefact class was excluded to calculate monthly lead fraction maps. This data is available on their website (http://meteo.uni-trier.de/arcleads.php). In this study, we compared the monthly lead fraction maps from January to March 2011 as AMSR-E based lead fraction maps were only available until 2011.

3. Methods

25   **3.1 Waveform mixture analysis**

Spectral linear mixture analysis assumes that the spectra measured by sensors for a pixel is a linear combination of the spectra of all components within the pixel (Keshava and Mustard. 2002). This technique is widely used to resolve spectral mixture problems in an image analysis (Foody and Cox, 1994; Dengsheng et al., 2003; Changshan. 2004; Iordache et al., 2011). Waveform mixture analysis is based on the concept of spectral linear mixture analysis. Since the waveform of altimetry within

30   a footprint could be considered to be a mixture of leads and various types of sea ice, linear mixture analysis can be applied in

this framework. In order to successfully implement waveform mixture analysis, the proper selection of an endmember is essential. The basic linear mixture model is defined as follows in equation 1.

$$Y_p = \sum_{k=1}^{K} a_{ik} E_k \qquad (1)$$

where $Y_p = \{Y_1, Y_2, Y_3, \ldots, Y_p\}$ represents waveform vectors and p means a bin in the waveform. a_{ik} is an abundance fraction,

5   which provides proportions in terms of endmember. E_k is the endmember vectors. Equation 1 is constrained under $\sum_{k=1}^{K} a_{ik} = 1$ and $a_{ik} \geq 0$. In this study, we used MATLAB toolbox for linear unmixing with the interior point least square algorithm provided by Chouzenoux et al. (2014) (http://www-syscom.univ-mlv.fr/~chouzeno/LogicielEN.html). This algorithm can handle huge data with inequality constraints, allowing reduced computational cost and high flexibility (Chouzenoux et al., 2014). While an endmember in remote sensing data represents a single pixel solely with a pure material, in this study,

10   waveforms of CryoSat-2 L1b data were used as endmembers such as the waveform of pure lead and first-year ice (FYI) (Fig. 1). Chase and Holyer (1990) were concerned by two problems with the application of linear mixture analysis to the waveform of altimeter data. First, the waveform within a footprint may not be linearly mixed between leads and sea ice. CryoSat-2 is more sensitive to the specular reflection of leads than the diffuse reflection of sea ice when both leads and sea ice exist within the same footprint, which implies the waveform may tend to be similar to the endmember of leads (Chase and Holyer. 1990).

15   The large number of range bins of CryoSat-2 could reduce the overestimation of leads. Secondly, the waveform of the altimeter (i.e., Geosat) is somewhat weighted on the centre of a footprint rather than representing an entire footprint. This could be an error source when applying linear mixture analysis to waveform data (Chase and Holyer. 1990). However, the CryoSat-2 L1b waveform is produced by averaging more than 200 weighted waveforms with various incidence angles, which can alleviate such a problem.

20   **3.2 Endmember selection**

The selection of endmembers is essential in the framework of waveform mixture analysis. We collected 48 CryoSat-2 files that traverse over the Arctic Ocean from January to May and from October to December 2011-2016 and extracted waveforms by using the decision trees (DT) algorithm developed for lead detection by Lee et al. (2016). DT has proven to be very effective in various remote sensing classification tasks (Lu et al., 2014; Li et al., 2013; Kim et al., 2015; Torbick and

25   Corbiere, 2015; Amani et al., 2017; Tadesse et al., 2017). Waveforms from March to April between 2011 and 2014 were compared to those from January to May, and October to December between 2011 and 2016 (not shown), resulting in little difference between them. This justified the use of the DT algorithm proposed by Lee et al. (2016) to extract waveform samples of leads and sea ice. The total number of sea ice and lead waveforms is 420,858 and 8,501, respectively. The N-FINDR algorithm was used in this study to select representative endmembers of leads and sea ice. N-FINDER uses an iterative simplex

30   volume expansion by endmembers, assuming that the volume defined by a simplex with pure pixels is always greater than any other combination of pixels, and thus the algorithm has been widely used for automatically selecting representative endmembers (Winter, 1999; Zortea and Plaza, 2009; Erturk and plaza, 2015; Ji et al., 2015; Chi et al., 2016). The lead

classification based on waveform mixture analysis was examined with 250 m MODIS images collected from March to May
and in October. It should be noted that since MODIS images with spatial resolution of 250 m were not available in January,
February, November, and December due to having polar nights, the evaluation with MODIS images and CryoSat-2 could not
be used. To secure the reliability of the comparison, the temporal difference between the MODIS images and CryoSat-2 data
5 was always under 30 minutes.

The waveform mixture model produces abundance data (i.e., lead and sea ice abundance) at along-track points with respect
to each endmember of the leads and sea ice. Thresholds have to be determined to make a binary classification between leads
and sea ice. Optimum thresholds to produce binary lead classification from lead and sea ice abundances were identified through
an automated calibration. To implement the automated calibration, reference point data of leads and sea ice were determined
10 by visual inspection of four MODIS images collected on 17 April 2014, 25 May 2015, 10 October 2015, and 27 March 2016.
While the calibration was conducted using half of the reference data randomly selected, the validation was performed using
the remaining data. Threshold combinations from 0.2 to 0.9 with a step size of 0.01, for both lead and sea ice abundances, were
tested and the one resulting in the highest accuracy was determined to be an optimum threshold combination.

Lead detection results were evaluated using three accuracy metrics—producer's accuracy, user's accuracy, and overall
15 accuracy. Producer's accuracy, which is associated with omission errors, is calculated as the percentage of correctly classified
pixels in terms of all reference samples for each class. User's accuracy, which is related to commission errors, is calculated as
the fraction of correctly classified pixels with regards to the pixels classified to a class. Overall accuracy is calculated as the
total number of correctly classified samples divided by the total number of validation sample data

A monthly lead fraction was derived by dividing the number of lead observations by the number of total observations
20 within a 10 km grid in a month. It is noted that while there are more than 30 CryoSat-2 observations in the 10 km grid around
the centre of the Arctic, CryoSat-2 observations less than 5 are in the 10 km grid around the coast line of Arctic Ocean. This
will be dealt with in the results section with more details.

3.3 Calculation of sensitivity in a 10x10 km grid

Since each grid has a different number of CryoSat-2 observations, a sensitivity analysis was conducted in terms of the
25 number of observations by grid. Thirty (30) percent of the number of lead and ice observations in 10x10 km grids was
repetitively permuted and the standard deviation of the resultant lead fractions through 50 iterations was calculated in grids.
The higher the standard deviation in a grid, the more sensitive the grid is to the change in the number of lead observations. It
should be noted that the standard deviation is zero when no lead observation is found, which means lead fraction is also zero.
Sensitivities were calculated from January to April 2011 because these months were used to compare the lead fractions from
30 the proposed waveform mixture analysis to those in the existing literature.

4 Results

4.1 Performance of lead classification

Fig. 1 shows representative waveforms of leads and sea ice extracted by the N-FINDR algorithm as endmembers. The waveform of leads is dominated by specular reflection, resulting in a narrow peak curve. The representative waveform of sea

5 ice has a wider distribution due to its rough surface when compared to that of leads. Considering different types of sea ice such as young ice, FYI, and Multi-Year Ice (MYI), the representative waveform of sea ice is similar to that of FYI (Zygmuntowska et al., 2013; Kurtz et al., 2014; Ricker et al., 2014; Wernecke and Kaleschke. 2015).

The optimum thresholds for the lead and sea ice abundances were determined to be 0.84 and 0.57 through the automated calibration, respectively. According to the thresholds, leads were identified with the conditions of lead abundance > 0.84 and

10 sea ice abundance < 0.57. Selected examples of lead detection results based on waveform mixture analysis are presented in Fig. 2 with threshold-based lead detection results from the existing literature (Rose, 2013; Laxon et al., 2013; and Lee et al., 2016). Simple thresholding approaches based on two waveform parameters, pulse peakiness (PP) and stack standard deviation (SSD) (i.e., PP > 0.25 and SSD < 4 for leads and PP < 0.45 and SSD > 4 for ice floes; PP > 18 and SSD < 4 for leads and PP < 9 and SSD > 4 for ice floes) were used in Rose (2013) and Laxon et al. (2013), respectively. It should be noted that since the

15 existing methods were developed using parameters such as beam behaviour parameters and backscatter sigma-0 extracted from baseline B data, rescaling was conducted on the parameters extracted from a newly updated baseline C data for reasonable comparison (Scagliola and Fornari, 2015).

Multiple lead classification methods based on CryoSat-2 data were assessed by visual inspection with high resolution (250m) MODIS images. The waveform mixture analysis produced better results than previous lead detection methods using

20 simple thresholding approaches such as Rose (2013) and Laxon et al. (2013) regardless of month (Fig. 2). While the performance of waveform mixture analysis was comparable to the DT algorithm from Lee et al. (2016), waveform mixture analysis slightly over-estimated leads resulting in lower user's accuracy than user's accuracy for leads by DT (Fig. 3). Lead classification results should be assessed during all the months (i.e., January to May, and October to December) and years (i.e., 2011 to 2016) using MODIS images to thoroughly evaluate the proposed waveform-based algorithm for lead detection.

25 However, lead classification results in January, February, November, and December were not assessed using MODIS images due to polar nights. Thus, the lead classification results in these months could possibly have uncertainties.
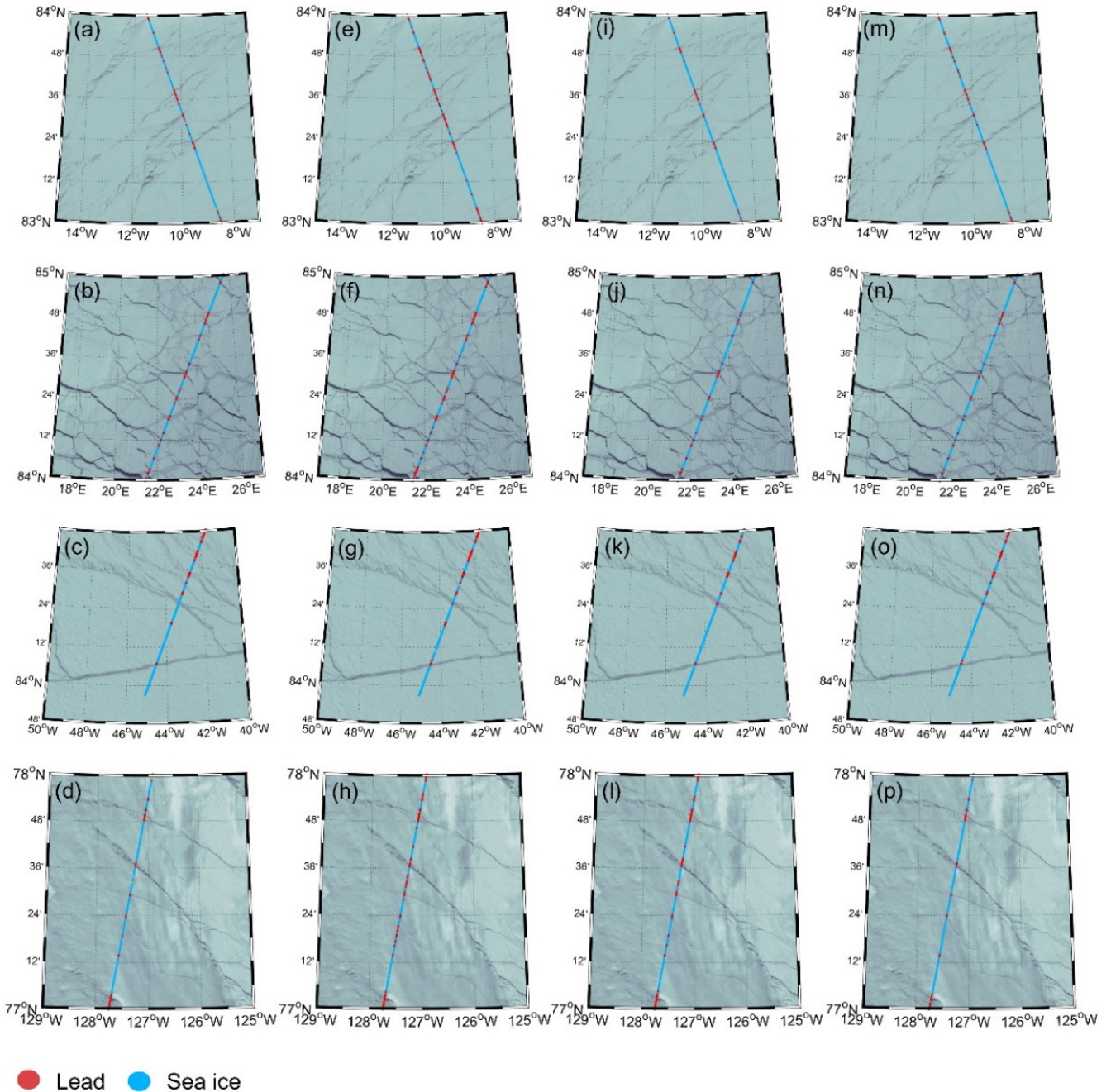
Figure 2: Visual comparison of lead classifications: (a) – (d) lead classifications based on Rose (2013), (e) – (h) lead classifications based on Laxon et al. (2013), (i) – (l) lead classifications based on decision trees from Lee et al. (2016), and (m) – (p) lead classifications based on the proposed waveform mixture analysis. The MODIS data were collected in March (a, e, i, and m), April (b, f, j, and n), May (c, g, k, and o), and October (d, h, l, and p).
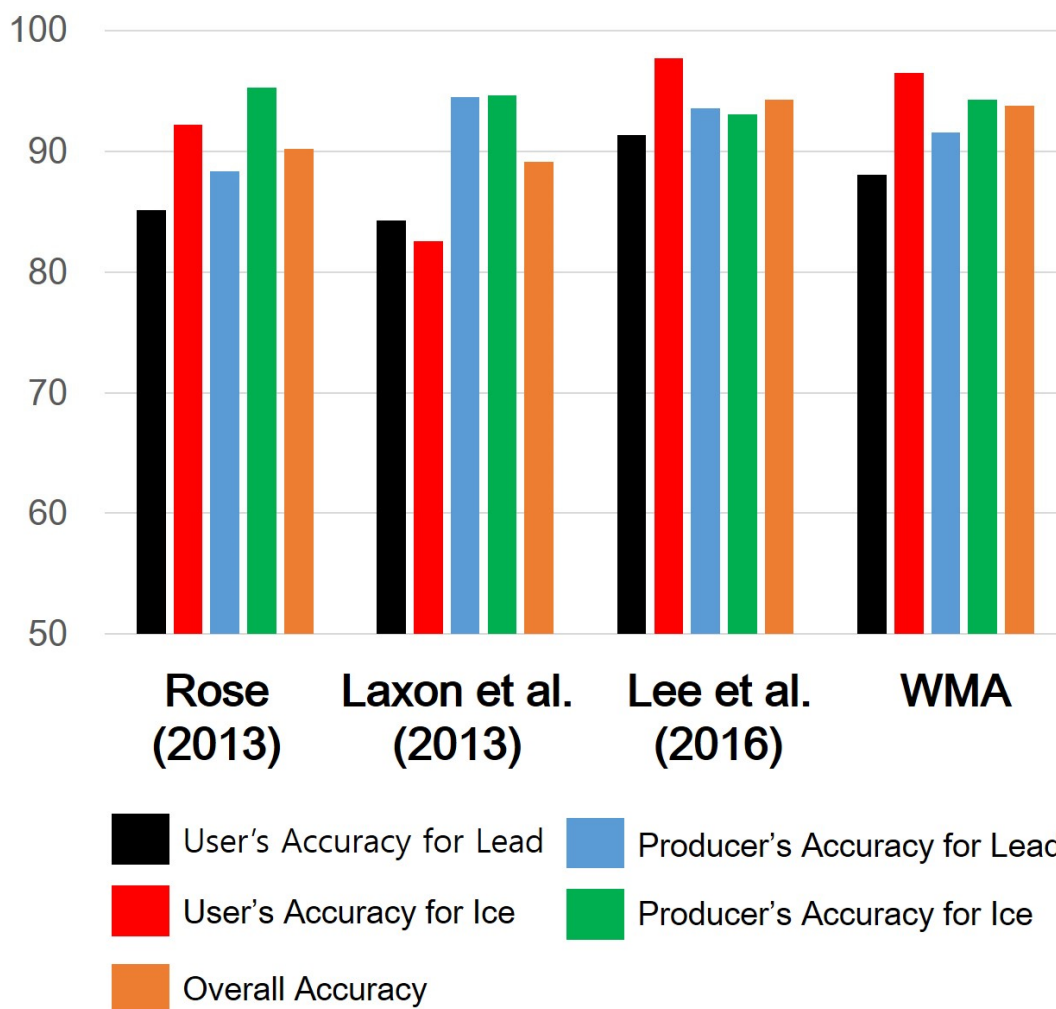
Figure 3: Accuracy assessment results for lead detection by method—three existing methods and the proposed waveform mixture analysis (WMA).

4.2 Spatiotemporal distribution of lead fraction maps

The monthly lead fraction maps in January to May, and October to December from 2011 to 2016 are shown in Figs. 4 and 5. The areas around the coast line of the Arctic Ocean clearly show higher lead fraction due to the shear zone and outflow of sea ice. In particular, high lead fraction was found around Beaufort Sea during the spring season (MAM) because of the Beaufort Gyre, a wind-driven ocean current. It is widely known that the Bering Strait is the main strait that warm Pacific water flows through into the Arctic (Woodgate et al., 2006; Woodgate et al., 2010). However, the lead fraction around the Chuckchi Sea was lower than the lead fraction around Beaufort Sea in March 2013 and 2016.

While the lead fraction decreases from October to March (i.e., freezing season) with the minimum in March (refer to Figs. 4c, k, s and Figs. 5c, k, s), the sea ice melting on the surface starts from April. This indicates an increasing lead fraction, which corresponds to the seasonal cycle of sea ice thickness. However, the lead fraction around the Beaufort Sea decreases in March and April of 2013 and 2016 (Figs. 4 and 5). The lead fraction in the spring season in 2013 was particularly high due to the sea

5 ice extent minimum in September 2012, which required a relatively long period of time to freeze up in the spring of 2013. December to January is usually considered as a freezing season. Nevertheless, the lead fraction around the central Arctic increased from December 2015 to January 2016. This result corresponds to the findings of Kim et al. (2017) and Ricker et al. (2017).
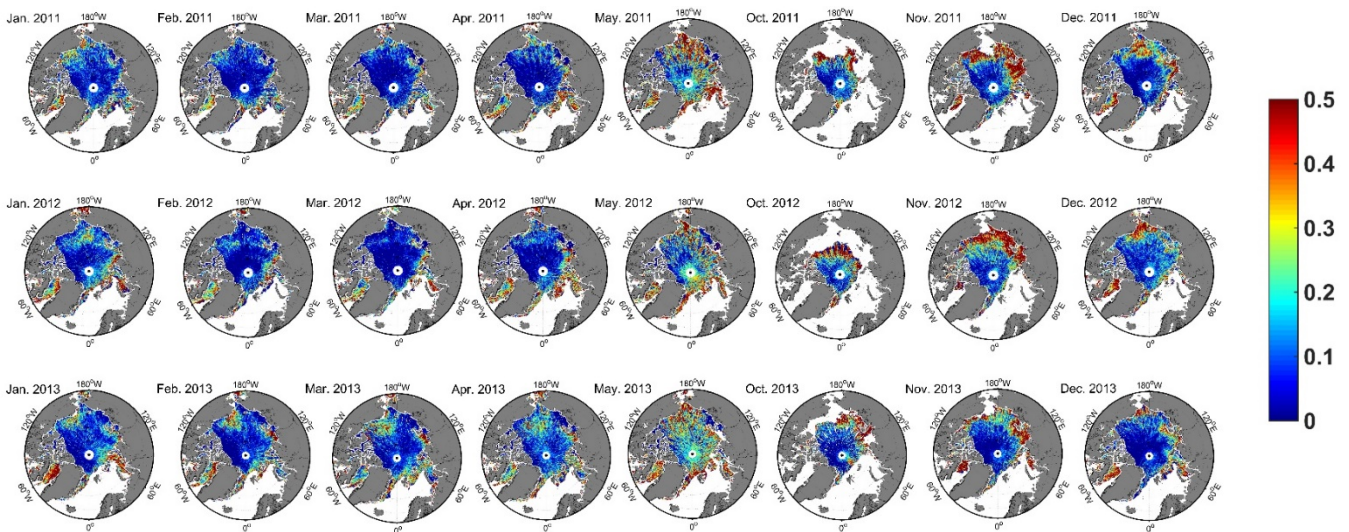
10 **Figure 4:** Monthly lead fraction maps based on waveform mixture analysis in January to May, October to December between 2011 and 2013. The range of the colour bar was set from 0 to 0.5 to emphasize lower values.
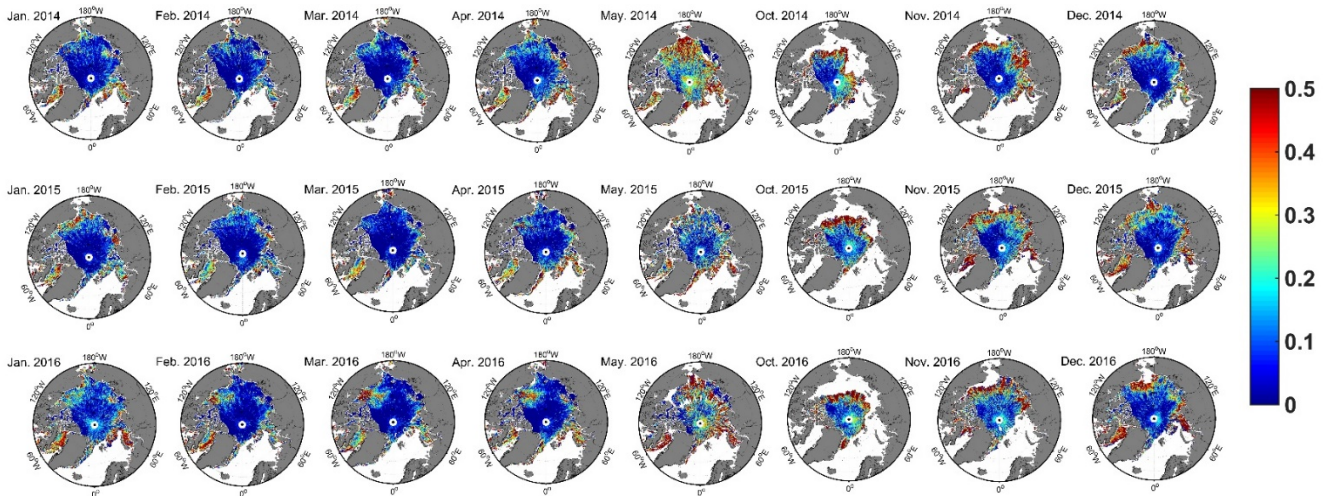
Figure 5: Monthly lead fraction maps based on waveform mixture analysis in January to May, October to December between 2014 and 2016. The range of the colour bar was set from 0 to 0.5 to emphasize lower values.

4.3 Grid sensitive analysis in 10x10 km

As mentioned in section 3.2, the number of CryoSat-2 observations decreases from the North Pole toward the coast line of Arctic Ocean. This results in an increase in uncertainties when calculating monthly lead fraction around the coast line of Arctic Ocean based on the small number of CryoSat-2 observations. The number of lead and ice observations is shown in Fig. 6a-h. While there are a few lead observations in the central Arctic, a large number of ice observations was found in the central Arctic. The high standard deviation values around the coast line of the Arctic Ocean zone imply that the reliability of lead fractions was low, while the relatively large number of CryoSat-2 observations around the North Pole produced low standard deviation indicating less uncertainty (Fig. 6i-l). There was spatial difference of uncertainty by month (i.e., January to April) because of the different number of lead observations. Especially, since there was no lead observation in the East Siberian coast and Eastern Laptev Sea, the sensitivity (i.e., standard deviation) was also zero (Fig. 6c and d). It should be noted that the corresponding lead fraction might not represent actual lead fraction in a 10 x 10 km grid. This is a drawback when calculating monthly lead fraction maps with satellite altimeters.

Number of lead observations
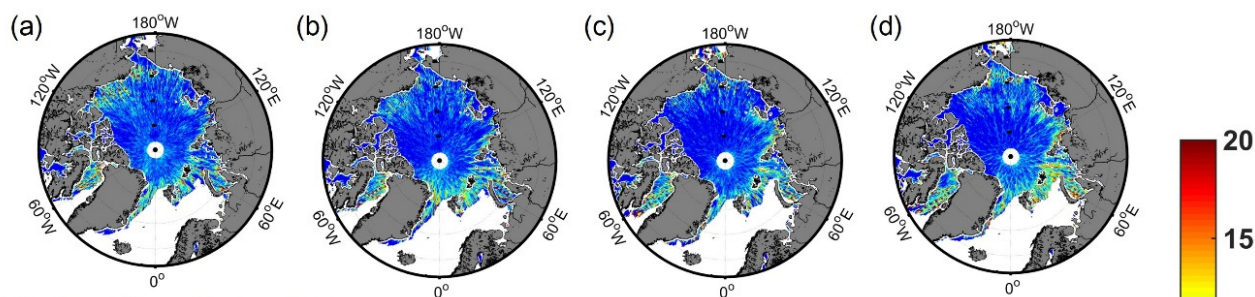
Number of ice observations
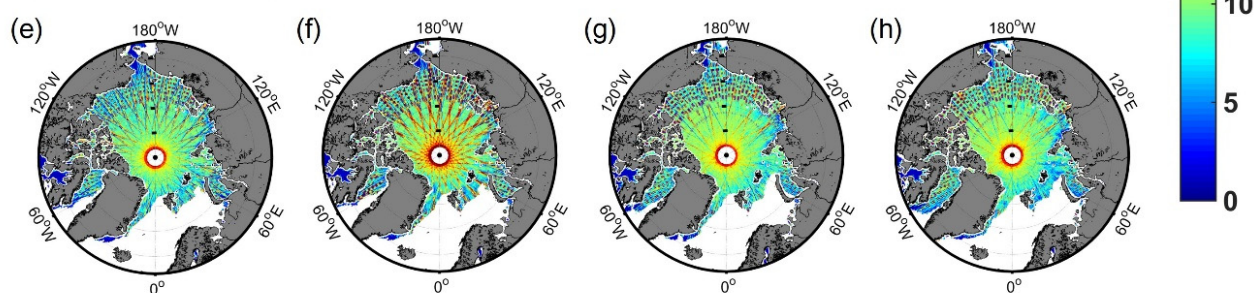
Standard deviation
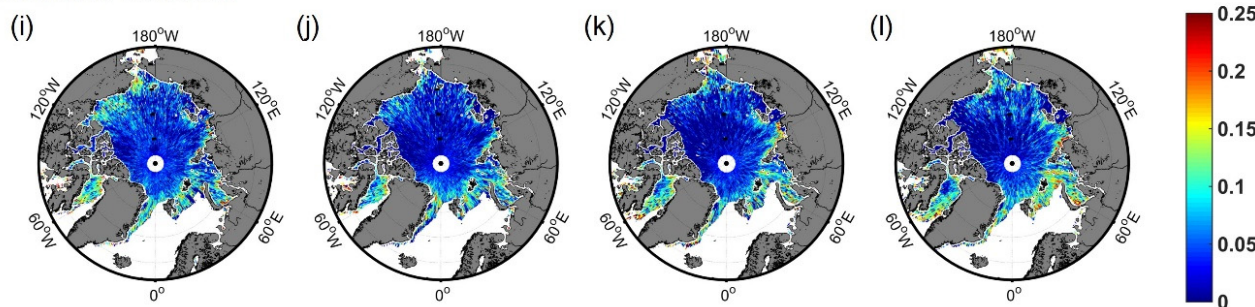
Figure 6: (a-d) the number of lead observations, (e-h) the number of ice observations, (i-l) the standard deviation of the results based on the sensitivity analysis of lead fraction from January to April 2011.

5. Discussion

5.1 Comparison of lead classification methods

While all classification methods produced high producer's accuracy for the ice class exceeding 93 %, the approaches from Lee et al. (2016) and Laxon et al. (2013) resulted in a bit higher producer's accuracy for leads than the other methods (Fig. 3). Although Laxon et al. (2013) produced the highest producer's accuracy for leads (i.e., 94.5 %), which means that this method

robustly detected leads, the user's accuracy for ice was the lowest, suggesting a huge number of false alarms for leads on the ice. Overestimation of leads may increase sea surface height anomaly (SSHA), which will lead to the underestimation of sea ice freeboard (Lee et al., 2016).

Since the overall accuracy metrics of the proposed waveform mixture analysis approach was comparable to those of the existing methods, especially DT, the waveform-based method can be used for estimating SSHA. Threshold-based lead detection methods have to be re-scaled whenever baseline data are updated. For example, beam behaviour parameters and backscatter sigma-0 changed slightly between when baseline B and baseline C data were used. Thus, thresholds must also be updated in order to appropriately identify leads using the threshold-based methods. However, waveform mixture analysis is free from the change of baseline data because waveforms can still be used to detect leads using updated baseline data. This is the strong point of waveform mixture analysis when compared to the existing methods.

The use of waveform mixture analysis might not work well to detect leads in cases of refreezing leads. In Figs. 2 c, g, k, and o, the dark area in the MODIS scenes around the latitude of 84.26°N and longitude of 43°W was determined to be a lead class with visual inspection of the images and waveforms. Rose (2013) classified this region as ice. Laxon et al. (2013) and waveform mixture analysis detected one lead in that region. In fact, since the leads were refrozen, the waveforms in that region were more similar to the typical FYI waveform. In the context of waveform mixture analysis, this region could be classified as ice. Therefore, in order to more accurately detect leads, a surface elevation anomaly is needed as well as beam behaviour parameters, backscatter sigma-0, and waveform mixture analysis.

5.2 Comparison to other lead fraction maps

Four monthly lead fraction maps (Rohrs and Kaleschke, 2012; Wernecke and Kaleschke, 2015; Willmes and Heinemann, 2016) were compared to evaluate the pros and cons of each method used to produce the maps (Fig. 7). Basically, all four methods represent the spatiotemporal pattern of leads well for the freezing season from January to March. Nonetheless, the spatial difference of lead fraction was found because different sensors with different spatial resolutions were used. Scene-based lead fraction maps (i.e., AMSR-E in Figs. 7a, b and c, and MODIS in Figs. 7d, e, and f) and altimeter-based lead fraction maps (i.e., CryoSat-2 in Figs. 7g to l) have fundamentally different spatial characteristics. Scene-based lead fraction maps better represent the linear feature of leads and coastal polynya than altimeter-based lead fraction maps. Since the AMSR-E-based approach only detects relatively large (~ 3 km) leads, lead fractions are generally lower than in the fraction maps using the other approaches. While altimeter-based lead fractions (Figs. 7g and j) in the Chuckchi Sea were high, scene-based lead fractions (Figs. 7a to f) were low in January 2011. There are pancake and nilas like sea ices in the Chukchi Sea, which is different from the general lead shape. Altimeter-based lead detection methods identified leads between pancake and nilas sea ices, generating a higher lead fraction in the Chukchi Sea. However, scene-based lead fraction methods did not detect leads in the Chuckchi Sea well, resulting in a lower lead fraction. The MODIS-based lead detection method that used ice surface

temperature (IST) did not detect leads in the Chukchi Sea (Figs. 8d, e, and f). In the AMSR-E images, sea ice signals were dominant in the footprint around the Chukchi Sea and cracks between pancake and nilas sea ices were identified as ice.

Altimeter-based monthly fraction maps might be insufficient to represent monthly lead fractions in the coast line of the Arctic Ocean due to the limited number of CryoSat-2 observations in a 10 km grid. Nonetheless, altimeter-based lead fraction

5   maps documented the overall spatial distribution of leads well, in particular, high lead fractions in the shear zone. Wernecke and Kaleschke (2015) used a random cross validation technique to derive optimum thresholds based on ground references (i.e., MODIS images). They identified leads conservatively to reduce false classifications. The classification results strongly depend on ground reference data. Since relatively high resolution (250m) MODIS images were used to construct reference data in this study, the waveform mixture analysis was able to identify small leads through the calibration process of the abundance data

10 (Fig. 2). Although the proposed waveform mixture analysis produced lead fraction maps with a higher spatial resolution than those in Wernecke and Kaleschke (2015), the lead fractions around the coast line of the Arctic Ocean from Wernecke and Kaleschke (2015) appeared to have less uncertainty. This is because of the larger number of lead observations in a much coarser grid than that from our results. The grid sensitivity analysis should be considered when interpreting the lead fraction maps around the coast line of the Arctic Ocean derived by the proposed waveform mixture analysis.

15 The choice of monthly lead fraction maps depends on the user's interest. Scene-based lead fraction maps better represent coastal polynya and the intrinsic form of leads (Rohrs and Kaleschke, 2012; Willmes and Heinemann, 2016). CryoSat-2 based lead fraction maps might not represent the linear shape of typical leads well like cracks which include pancake and nilas sea ices that are not in linear form. This is also a way to exchange heat and momentum transfer between the atmosphere and ocean, which can be detected as leads.
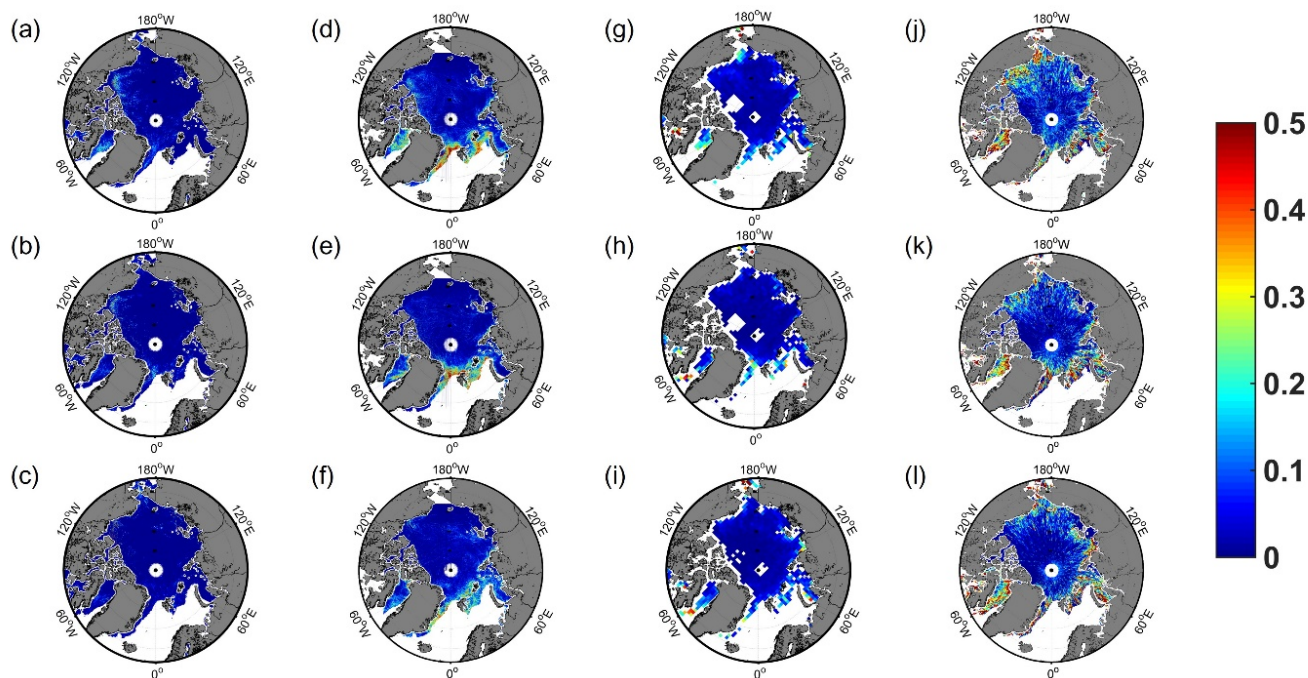
Figure 7: Comparison to other lead fraction maps in January to March 2011. (a-c) Monthly mean thin ice concentration maps using AMSR-E from Rohrs and Kaleschke (2011). (d-f) Monthly mean lead fraction maps using MODIS from Willmes and Heinemann (2015). (g-i) Monthly lead fraction maps using CryoSat-2 from Wernecke and Kaleschke (2015). (j-l) Monthly lead fraction maps based on waveform mixture analysis using Cryosat-2 in this study.

5.3 Lead dynamics

The features of the Arctic sea ice dynamics are driven by wind and, to a lesser degree, ocean currents (Kwok and Untersteiner, 2011). The Arctic Ocean circulations have contributed to the change in the state of sea ice. The two major circulations: the western Beaufort Gyre and Transpolar Drift in the Arctic, lead to high lead fraction around the Beaufort Sea and Fram Strait. The lead fraction in northwestern Greenland in Fig. 7 is low because of the convergence of sea ice by two major circulations, which was clearly shown in Kwok (2015). Kwok et al. (2013) revealed that the currents speed of Beaufort Gyre and Transpolar Drift increased from the years of 1982 to 2009 and this makes the fraction of multi-year ice decrease. However, the increasing trend of lead fraction from the years of 2011 to 2016 in this study was not seen due to the high inter-annual variability of lead fraction, particularly in the spring season (Fig. 8). High uncertainties in the marginal sea ice zone might result in not catching the increasing trend of Arctic lead fraction shown in the literature. In order to properly compare the Arctic current circulations and lead fraction, long-term lead fraction data are needed.

The inter-annual variability of lead fraction is related to atmospheric anomalous phenomena. Lead fraction suddenly decreased from March and April 2013 to 2014 (Figs. 4 and 5). This unexpected decrease of lead fraction corresponds to the

increase in sea ice thickness. Tilling et al. (2015) assessed the main cause of increase of sea ice thickness to be an anomalous cool summer in 2013. While November to March is considered to be the freezing season, the lead fraction increased in the central Arctic between December 2015 and January 2016 (Fig. 5). Kim et al. (2017) and Ricker et al. (2017) explained a plausible reason for the reduction in sea ice growth. Warm and moist air from the Atlantic Ocean strongly intruded into the

5 Arctic, weakening sea ice growth. Furthermore, the high lead fraction in the Beaufort Sea in February to April 2016 was attributable to the high ice drift speed (Ricker et al., 2017).
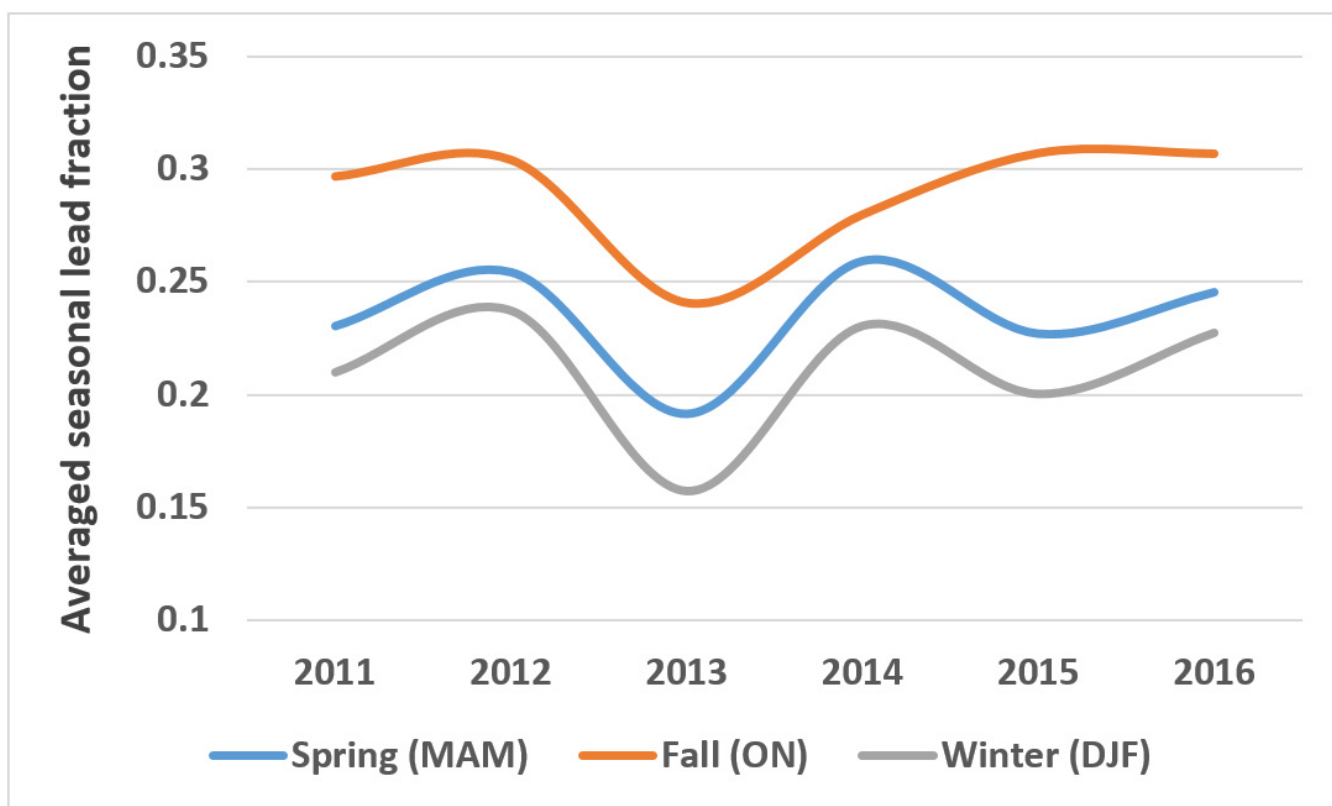
Figure 8: Averaged seasonal lead fraction in spring (MAM), fall (ON), and winter (DJF) between 2011 and 2016. The lead fraction from June to September was not available because leads were hard to distinguish from melt ponds using CryoSat-2 in the summer season.

6. Novelty and limitations

In this study, we developed an alternative lead detection method (i.e., waveform mixture analysis) using CryoSat-2 L1b data, which can overcome the drawbacks of previous threshold based lead detection methods. Regardless of an update in CryoSat-2 baseline data, the proposed waveform mixture analysis can consistently identify leads without rescaling parameters

15 such as beam behaviour parameters, pulse peakiness, and backscatter sigma-0. Such parameters must be rescaled to implement

threshold based lead detection methods when using updated CryoSat-2 baseline data. In addition, the proposed waveform mixture analysis outperformed the existing simple thresholding-based methods (Rose, 2013; Laxon et al., 2013), and was comparable to the machine learning-based thresholding method (Lee et al., 2016). In addition, this study showed the high inter-annual variability of Pan-Arctic lead fractions in recent years (i.e., 2011-2016), which implies that sea ice becomes more

5   vulnerable to atmospheric and oceanic forcing.

On the other hand, the waveform mixture analysis depends on the quality of the endmembers. Although the use of the N-FINDR algorithm decreased the subjective selection of endmembers, waveform samples of leads and sea ice derived by DT algorithm from Lee et al. (2016) may introduce uncertainty because the algorithm was validated for March and April from 2011 to 2014. The spatial resolution of monthly lead fraction maps improved up to 10km, showing detailed spatial distribution

10   of leads in the Arctic. However, a few CryoSat-2 observations in 10 km grids, especially around coast line of the Arctic Ocean, could cause uncertainty about lead fractions.

7. Conclusions

The waveform mixture analysis was proposed to detect leads with CryoSat-2 L1b data. The lead and sea ice waveforms

15   were considered as endmembers that are essential to implement waveform mixture analysis. The endmembers (i.e., representative waveforms of leads and sea ice) were extracted by the N-FINDR algorithm among numerous waveforms (i.e., 420,858 waveforms of sea ice and 8,501 waveforms of leads). The thresholds to make a binary classification were determined by calibrating lead and sea ice abundances with reference data extracted from high resolution (250m) MODIS images. The results show that the proposed approach robustly classified leads regardless of the month with better performance than previous

20   simple thresholding approaches for lead detection (Rose 2013; Laxon et al., 2013). Furthermore, the lead detection of waveform mixture analysis was comparable to the decision tree based lead detection method (Lee et al., 2016), suggesting a sea ice freeboard can be retrieved with the robust lead detection method using waveform mixture analysis. Monthly lead fraction maps were produced using the proposed waveform mixture approach, showing clear inter-annual variability. Scene-based lead fraction maps have different characteristics from altimeter-based lead fraction maps due to different sensors,

25   algorithms, and spatial resolutions but showed similar spatial distribution. The results of the lead fraction maps are consistent with the findings of recent studies (Tilling et al., 2015; Ricker et al., 2017; Kim et al., 2017). The lead dynamics based on monthly lead fraction maps were examined with the Arctic Atmospheric and oceanic circulations.

Unlike thresholds based lead detection methods, the waveform mixture analysis is free from the update of baseline version of CryoSat-2 data, which will be useful for future altimeter missions. The recent strong inter-annual variability of Arctic sea

ice conditions was found. In this context, this waveform mixture analysis can be used to consistently produce monthly lead fraction maps during the extended CryoSat-2 mission for monitoring Arctic sea ice.

Acknowledgements

5   This study was supported by the Korea Polar Research Institute (KOPRI) grant PE170120 (Research on analytical techniques for satellite observations of Arctic sea ice).

References

Aaboe, S., Breivik, L., Sorensen, A., Eastwood, S., and Lavergne, T.: Global Sea Ice Edge and Type Product User's Manual, EUMETSAT OSISAF, 2016.

10   Amani, M., Salehi, B., Mahdavi, S., Granger, J., Brisco, B.: Wetland classification in Newfoundland and Labrador using multi-source SAR and optical data integration. GIScience and Remote Sensing, in press, 2017.

Bröhan, D., and Kaleschke, L.: A Nine-Year Climatology of Arctic Sea Ice Lead Orientation and Frequency from AMSR-E, Remote Sensing, 6, 1451, 2014.

Chase, J. R., and Holyer, R. J.: Estimation of sea ice type and concentration by linear unmixing of Geosat altimeter waveforms,

15   Journal of Geophysical Research: Oceans, 95, 18015-18025, 10.1029/JC095iC10p18015, 1990.

Chi, J., Kim, H.-C., and Kang, S.-H.: Machine learning-based temporal mixture analysis of hypertemporal Antarctic sea ice data, Remote Sensing Letters, 7, 190-199, 10.1080/2150704X.2015.1121300, 2016.

Chouzenoux, E., Legendre, M., Moussaoui, S., and Idier, J.: Fast Constrained Least Squares Spectral Unmixing Using Primal-Dual Interior-Point Optimization, IEEE Journal of Selected Topics in Applied Earth Observations and Remote Sensing,

20   7, 59-69, 10.1109/JSTARS.2013.2266732, 2014.

Ertürk, A., and Plaza, A.: Informative Change Detection by Unmixing for Hyperspectral Images, IEEE Geoscience and Remote Sensing Letters, 12, 1252-1256, 10.1109/LGRS.2015.2390973, 2015.

Foody, G. M., and Cox, D. P.: Sub-pixel land cover composition estimation using a linear mixture model and fuzzy membership functions, Remote sensing, 15(3), 619-631, 1994.

25   Iordache, M. D., Bioucas-Dias, J. M., and Plaza, A.: Sparse Unmixing of Hyperspectral Data, IEEE Transactions on Geoscience and Remote Sensing, 49, 2014-2039, 10.1109/TGRS.2010.2098413, 2011.

Janout, M. A., Aksenov, Y., Hölemann, J. A., Rabe, B., Schauer, U., Polyakov, I. V., Bacon, S., Coward, A. C., Karcher, M., Lenn, Y.-D., Kassens, H., and Timokhov, L.: Kara Sea freshwater transport through Vilkitsky Strait: Variability, forcing, and further pathways toward the western Arctic Ocean from a model and observations, Journal of Geophysical Research:

30   Oceans, 120, 4925-4944, 10.1002/2014JC010635, 2015.

Ji, L., Geng, X., Sun, K., Zhao, Y., and Gong, P.: Modified N-FINDR endmember extraction algorithm for remote-sensing

imagery, International Journal of Remote Sensing, 36, 2148-2162, 10.1080/01431161.2015.1034895, 2015.

Keshava, N., and Mustard, J. F.: Spectral unmixing, IEEE Signal Processing Magazine, 19, 44-57, 10.1109/79.974727, 2002.

Key, J., Stone, R., Maslanik, J., and Ellefsen, E.: The detectability of sea-ice leads in satellite data as a function of atmospheric conditions and measurement scale, Annals of Glaciology, 17, 227-232, 10.3198/1993AoG17-1-227-232, 1993.

5   Rose, S., Forsberg, R., and Pedersen, L.: Measurements of sea ice by satellite and airborne altimetry, DMIDMI,

Kim, B.-M., Hong, J.-Y., Jun, S.-Y., Zhang, X., Kwon, H., Kim, S.-J., Kim, J.-H., Kim, S.-W., and Kim, H.-K.: Major cause of unprecedented Arctic warming in January 2016: Critical role of an Atlantic windstorm, Scientific Reports, 7, 40051, 10.1038/srep40051, http://www.nature.com/articles/srep40051#supplementary-information, 2017.

Kim, M., Im, J., Han, H., Kim, J., Lee, S., Shin, M., Kim, H.-C. Landfast sea ice monitoring using multisensor fusion in the
10   antarctic. *GIScience & Remote Sensing*, *52*, 239-256, 2015.

Kurtz, N. T., Galin, N., and Studinger, M.: An improved CryoSat-2 sea ice freeboard retrieval algorithm through the use of waveform fitting, The Cryosphere, 8, 1217-1237, 10.5194/tc-8-1217-2014, 2014.

Kwok, R., and Untersteiner, N.: The thinning of Arctic sea ice, Physics today, 64(4), 36-41. 2011.

Kwok, R., Spreen, G., and Pang, S.: Arctic sea ice circulation and drift speed: Decadal trends and ocean currents, Journal of
15   Geophysical Research: Oceans, 118, 2408-2425, 10.1002/jgrc.20191, 2013.

Kwok, R.: Sea ice convergence along the Arctic coasts of Greenland and the Canadian Arctic Archipelago: Variability and extremes (1992–2014), Geophysical Research Letters, 42, 7598-7605, 10.1002/2015GL065462, 2015.

Lüpkes, C., Vihma, T., Birnbaum, G., and Wacker, U.: Influence of leads in sea ice on the temperature of the atmospheric boundary layer during polar night, Geophysical Research Letters, 35, n/a-n/a, 10.1029/2007GL032461, 2008.

20 Laxon, S. W., Giles, K. A., Ridout, A. L., Wingham, D. J., Willatt, R., Cullen, R., Kwok, R., Schweiger, A., Zhang, J., Haas, C., Hendricks, S., Krishfield, R., Kurtz, N., Farrell, S., and Davidson, M.: CryoSat-2 estimates of Arctic sea ice thickness and volume, Geophysical Research Letters, 40, 732-737, 10.1002/grl.50193, 2013.

Lee, S., Im, J., Kim, J., Kim, M., Shin, M., Kim, H.-c., and Quackenbush, L.: Arctic Sea Ice Thickness Estimation from CryoSat-2 Satellite Data Using Machine Learning-Based Lead Detection, Remote Sensing, 8, 698, 2016.

25 Li, M., Im, J., Beier, C. Machine learning approaches for forest classification and change analysis using multi-temporal landsat tm images over huntington wildlife forest. *GIScience & Remote Sensing, 50*, 361-384, 2013.

Lindsay, R. W., and Rothrock, D. A.: Arctic sea ice leads from advanced very high resolution radiometer images, Journal of Geophysical Research: Oceans, 100, 4533-4544, 10.1029/94JC02393, 1995.

Lu, Z., Im, J., Rhee, J., Hodgson, M. Building type classification using spatial and landscape attributes derived from lidar
30   remote sensing data. *Landscape and Urban Planning, 130*, 134-148, 2014.

Marcq, S., and Weiss, J.: Influence of sea ice lead-width distribution on turbulent heat transfer between the ocean and the atmosphere, The Cryosphere, 6, 143-156, 10.5194/tc-6-143-2012, 2012.

Maykut, G. A.: Energy exchange over young sea ice in the central Arctic, Journal of Geophysical Research: Oceans, 83(C7), 3646-3658, 1978.

Maykut, G. A.: Large-scale heat exchange and ice production in the central Arctic, Journal of Geophysical Research: Oceans, 87, 7971-7984, 10.1029/JC087iC10p07971, 1982.

Miles, M. W., and Barry, R. G.: A 5-year satellite climatology of winter sea ice leads in the western Arctic, Journal of Geophysical Research: Oceans, 103(C10), 21723-21734, 1998

Overland, J. E., Francis, J. A., Hanna, E., and Wang, M.: The recent shift in early summer Arctic atmospheric circulation, Geophysical Research Letters, 39, n/a-n/a, 10.1029/2012GL053268, 2012.

Perovich, D. K., Jones, K. F., Light, B., Eicken, H., Markus, T., Stroeve, J., and Lindsay, R.: Solar partitioning in a changing Arctic sea-ice cover, Annals of Glaciology, 52(57), 192-196, 2011

Röhrs, J., and Kaleschke, L.: An algorithm to detect sea ice leads by using AMSR-E passive microwave imagery, The Cryosphere, 6, 343-352, 10.5194/tc-6-343-2012, 2012.

Ricker, R., Hendricks, S., Helm, V., Skourup, H., and Davidson, M.: Sensitivity of CryoSat-2 Arctic sea-ice freeboard and thickness on radar-waveform interpretation, The Cryosphere, 8, 1607-1622, 10.5194/tc-8-1607-2014, 2014.

Ricker, R., Hendricks, S., Girard-Ardhuin, F., Kaleschke, L., Lique, C., Tian-Kunze, X., Nicolaus, M., and Krumpen, T.: Satellite-observed drop of Arctic sea-ice growth in winter 2015-2016, Geophysical Research Letters, n/a-n/a, 10.1002/2016GL072244, 2017.

Salvatore D.: Guidelines for reverting Waveform Power to Sigma Nought for CryoSat-2 in SAR mode, European Space Agency, 2014.

Scagliola, M., and Fornari, M.: Main evolutions and expected quality improvements in BaselineC Level1b products (No. 1.3), C2-TN-ARS-GS-5154, 2015.

Spall, M. A.: Circulation and water mass transformation in a model of the Chukchi Sea, Journal of Geophysical Research: Oceans, 112, n/a-n/a, 10.1029/2005JC003364, 2007.

Tilling, R. L., Ridout, A., Shepherd, A., and Wingham, D. J.: Increased Arctic sea ice volume after anomalously low melting in 2013, Nature Geosci, 8, 643-646, 10.1038/ngeo2489 http://www.nature.com/ngeo/journal/v8/n8/abs/ngeo2489.html#supplementary-information, 2015.

Tadesse, T., Champagne, C., Wardlow, B., Hadwen, T., Brown, J., Demisse, G., Bayissa, Y., Davidson, A.: Building the vegetation drought response index for Canada (BegDRI-Canada) to monitor agricultural drought: first results. GIScience and Remote Sensing, 54(2), 230-257, 2017.

Torbick, N., Corbiere, M.: Mapping urban sprawl and impervious surfaces in the northeast United States for the past four decades. *GIScience & Remote Sensing, 52*(6), 746-764, 2015.

Weingartner, T., Aagaard, K., Woodgate, R., Danielson, S., Sasaki, Y., and Cavalieri, D.: Circulation on the north central Chukchi Sea shelf, Deep Sea Research Part II: Topical Studies in Oceanography, 52, 3150-3174, http://doi.org/10.1016/j.dsr2.2005.10.015, 2005.

Wernecke, A., and Kaleschke, L.: Lead detection in Arctic sea ice from CryoSat-2: quality assessment, lead area fraction and width distribution, The Cryosphere, 9, 1955-1968, 10.5194/tc-9-1955-2015, 2015.

Willmes, S., and Heinemann, G.: Pan-Arctic lead detection from MODIS thermal infrared imagery, Annals of Glaciology, 56(69), 29-37, 2015

Willmes, S., and Heinemann, G.: Sea-Ice Wintertime Lead Frequencies and Regional Characteristics in the Arctic, 2003–2015, Remote Sensing, 8, 4, 2016.

5 Wingham, D. J., Francis, C. R., Baker, S., Bouzinac, C., Brockley, D., Cullen, R., de Chateau-Thierry, P., Laxon, S. W., Mallow, U., Mavrocordatos, C., Phalippou, L., Ratier, G., Rey, L., Rostan, F., Viau, P., and Wallis, D. W.: CryoSat: A mission to determine the fluctuations in Earth's land and marine ice fields, Advances in Space Research, 37, 841-871, http://dx.doi.org/10.1016/j.asr.2005.07.027, 2006.

Winter, M. E.: N-FINDR: an algorithm for fast autonomous spectral end-member determination in hyperspectral data, 1999,
10   266-275,

Woodgate, R. A., Aagaard, K., and Weingartner, T. J.: Interannual changes in the Bering Strait fluxes of volume, heat and freshwater between 1991 and 2004, Geophysical Research Letters, 33, n/a-n/a, 10.1029/2006GL026931, 2006.

Woodgate, R. A., Weingartner, T., and Lindsay, R.: The 2007 Bering Strait oceanic heat flux and anomalous Arctic sea-ice retreat, Geophysical Research Letters, 37, n/a-n/a, 10.1029/2009GL041621, 2010.

15 Wu, C.: Normalized spectral mixture analysis for monitoring urban composition using ETM+ imagery, Remote Sensing of Environment, 93(4), 480-492, 2004.

Zakharova, E. A., Fleury, S., Guerreiro, K., Willmes, S., Rémy, F., Kouraev, A. V., and Heinemann, G.: Sea Ice Leads Detection Using SARAL/AltiKa Altimeter, Marine Geodesy, 38, 522-533, 10.1080/01490419.2015.1019655, 2015.

Zortea, M., and Plaza, A.: A Quantitative and Comparative Analysis of Different Implementations of N-FINDR: A Fast
20   Endmember Extraction Algorithm, IEEE Geoscience and Remote Sensing Letters, 6, 787-791, 10.1109/LGRS.2009.2025520, 2009.

Zygmuntowska, M., Khvorostovsky, K., Helm, V., and Sandven, S.: Waveform classification of airborne synthetic aperture radar altimeter over Arctic sea ice, The Cryosphere, 7, 1315-1324, 10.5194/tc-7-1315-2013, 2013.

25